ROSE-HULMAN INSTITUTE OF TECHNOLOGY

CHEMISTRY AND BIOCHEMISTRY

Implications of Influenza Properties

(No! Don't sneeze on me . . .)

Seasonal Behavior of Influenza

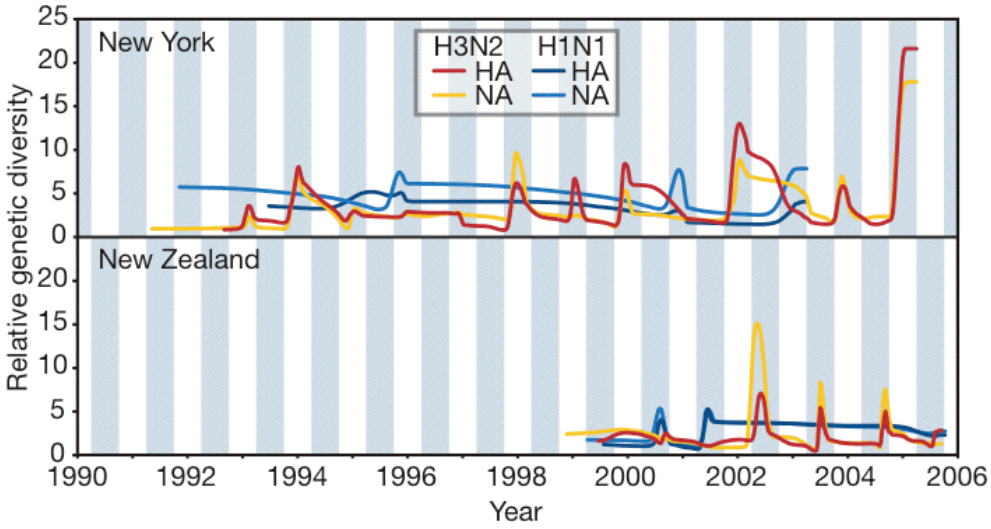

Figure 1 | Population dynamics of genetic diversity in influenza A virus. Bayesian skyline plots of the HA and NA segments for the A/H3N2 and A/H1N1 subtypes in New York state (top) and New Zealand (bottom). The horizontal shaded blocks represent the winter seasons. The *y*-axes represent a measure of relative genetic diversity (see Methods for details). The shorter timescale of New Zealand skyline plot is due to the shorter sampling period.

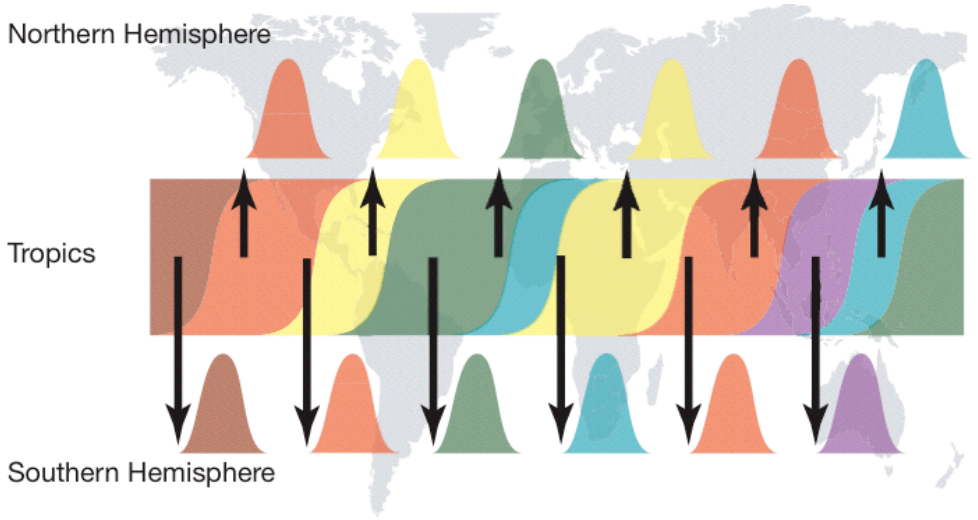

Figure 2 | A 'source–sink' model for the evolution of influenza A virus. Viral genetic and antigenic diversity (shown by different colours) is continuously generated in a reservoir, or 'source' population, perhaps represented by the tropics, before being exported to 'sink' populations in the Northern and Southern Hemispheres as shown by the arrows. The continuous transmission of influenza A virus in the source population, and hence its larger effective population size, allows natural selection for antigenic diversity to proceed more efficiently than in the sink populations that are afflicted by major seasonal bottlenecks.

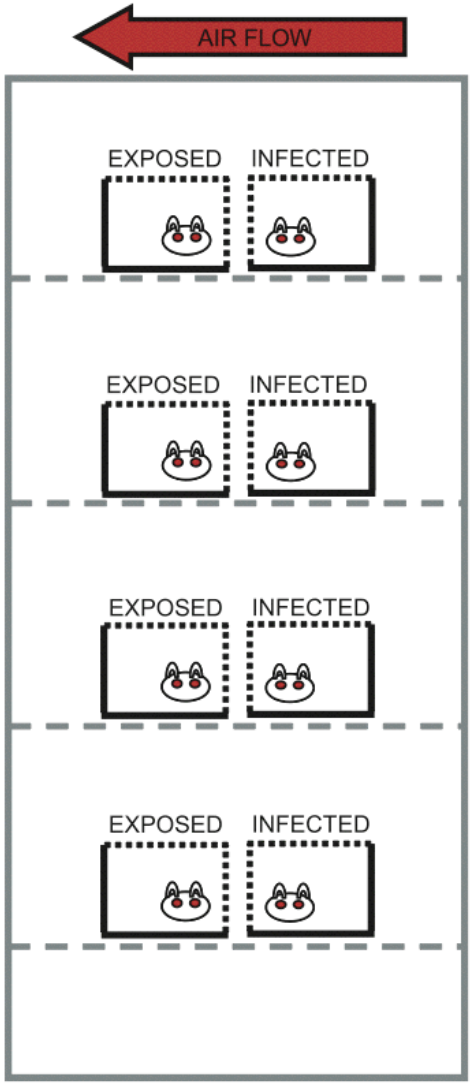

Figure 1. Arrangement of Infected and Exposed Guinea Pigs in Environmental Chamber

In each experiment, eight animals were housed in a Caron 6030 environmental chamber. Each guinea pig was placed in its own cage, and two cages were positioned on each shelf. Naïve animals were placed behind infected animals, such that the direction of airflow was toward the naïve animals. The cages used were open to airflow through the top and one side, both of which were covered by wire mesh. Although infected and exposed guinea pigs were placed in pairs, air flowed freely between shelves, allowing transmission to occur from any infected to any naïve animal.

doi:10.1371/journal.ppat.0030151.g001

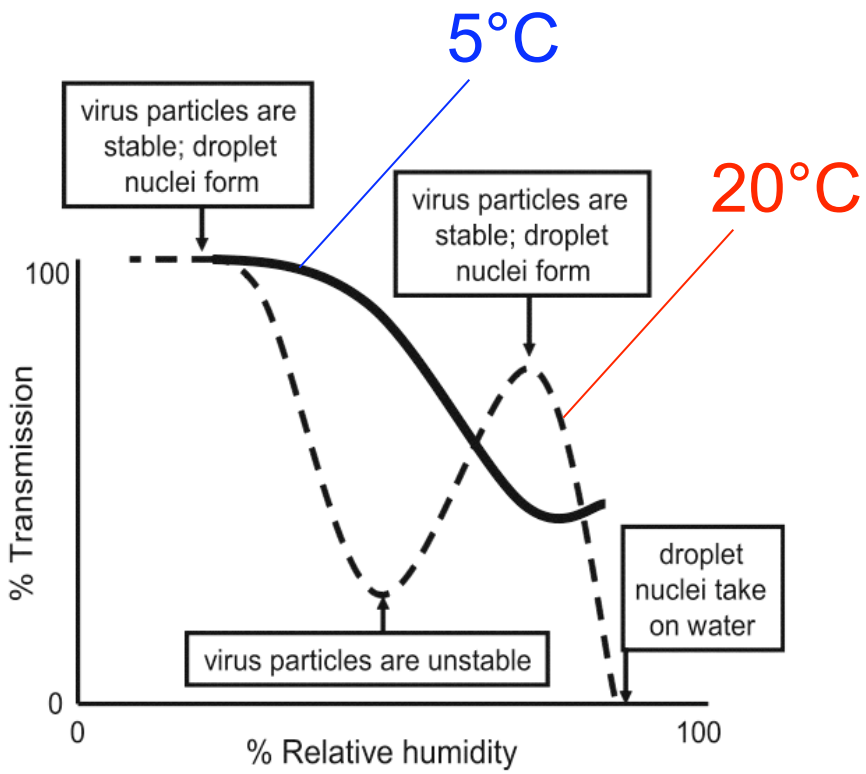

Figure 6. Variation of Transmission Efficiency with Relative Humidity: A Model

At 20 °C (dashed line), transmission efficiency is highest at low RH, when influenza virions in an aerosol are relatively stable, and desiccation of exhaled respiratory droplets produces droplet nuclei. Transmission is diminished at intermediate RH when virus particles are relatively unstable, but improves in parallel with influenza virus stability at higher humidities. At high RH, evaporation from exhaled particles is limited, respiratory droplets settle out of the air, and transmission is blocked. At 5 °C (solid line), transmission is more efficient than at 20 °C, but is reduced to a rate of 50% at higher humidities.

doi:10.1371/journal.ppat.0030151.g006

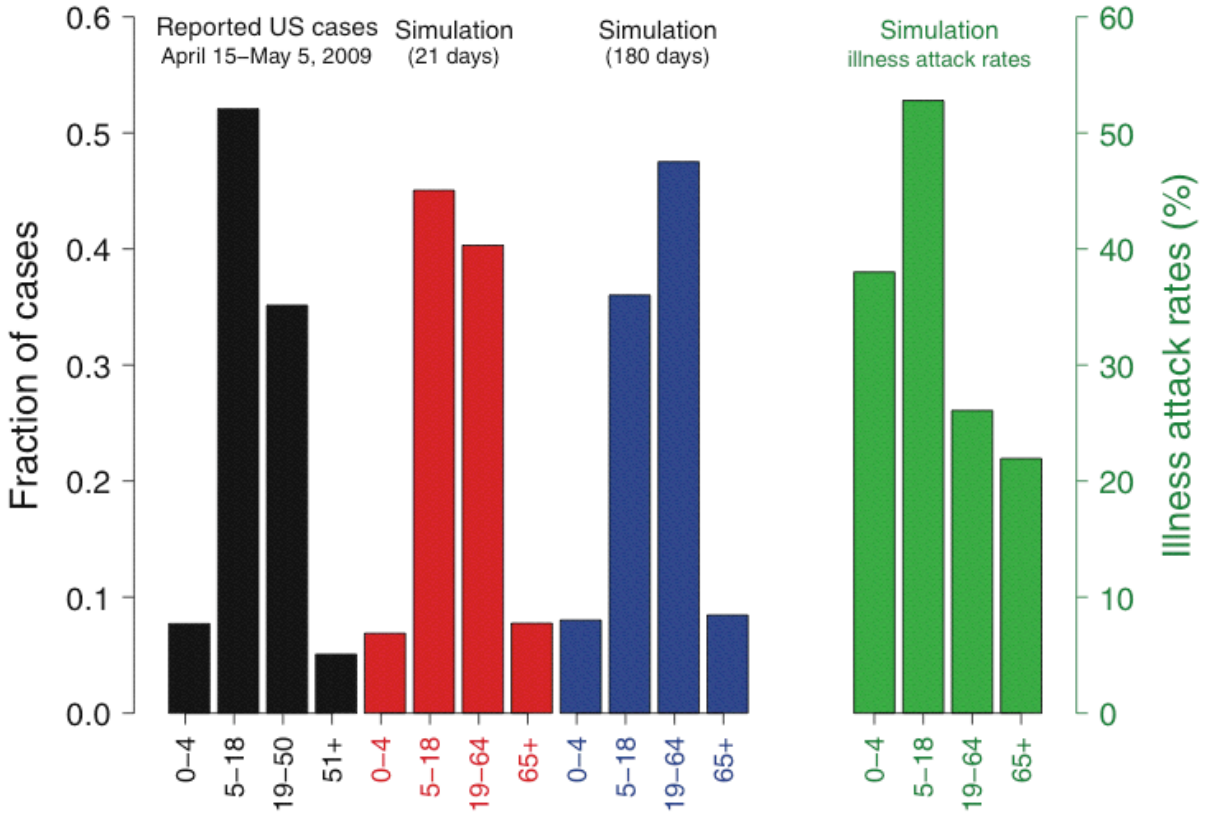

Fig. 2. Observed and simulated age-specific fraction of influenza cases and illness attack rates, with R_0 = 1.6. The black bars show the observed proportion of reported pandemic H1N1 cases by age group in the United States during the early days of the reported U.S. epidemic. The red and blue bars show the simulated proportion at different times after introduction of cases into the Los Angeles County area. The age distribution of cases at 21 days of the simulated epidemic is similar to that of the early observed epidemic. As reflected in the later epidemic, older age groups would become more involved as the infections spreads beyond schools and households. The green bars show the simulated age-specific illness attack rates by the end of an epidemic that runs to completion in the Los Angeles County area. This final age-specific attack rate pattern is similar to that observed for the 1957–1958 Asian A (H2N2) pandemic (*37*).

Pandemic transmissibility

	low			*moderate*			*high*					
R_0	1.3	1.4	1.5	1.6	1.7	1.8	1.9	2.0	2.1	2.2	2.3	2.4
Illness attack rate (%)	21	26	29	32	35	38	40	42	44	46	48	49
Global cases (billions)	1.4	1.7	2.0	2.2	2.4	2.6	2.7	2.9	3.0	3.1	3.2	3.3

Fig. 3. Simulated illness attack rate for the United States and projected total number of global cases for 1 year of pandemic influenza at different values of R_0. The projections were obtained by multiplying the simulated illness attack rates by the world population of 6.8 billion.

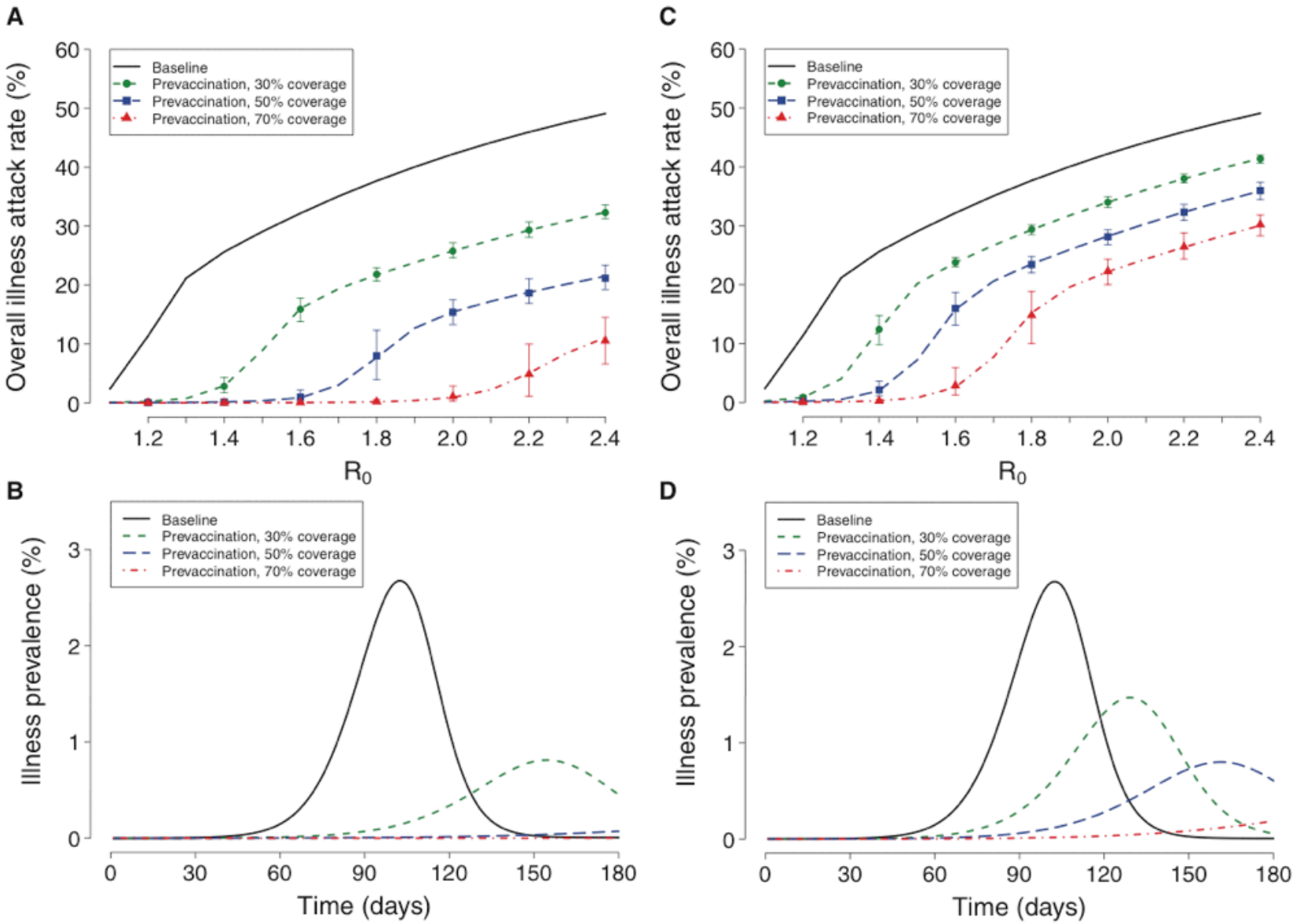

Fig. 4. Simulated effect of prevaccination with a homologously and a heterologously matched pandemic influenza vaccine at different values of R_0 and coverage for the United States. (**A**) Overall illness attack rates for homologous vaccine. Lines indicate the average illness attack rate over five simulations of Los Angeles County for each value of R_0 with the vaccine efficacies summarized in table S9. The 95% error bars indicate the empirical confidence intervals for 100 simulations where the vaccine efficacy parameters are chosen randomly within 15% of their estimated values. (**B**) Epidemic curves at $R_0 = 1.6$ with homologous vaccine. (**C**) Overall illness attack rates with a heterologous vaccine and 95% error bars indicating the empirical confidence intervals when varying the vaccine efficacy parameters. (**D**) Epidemic curves at $R_0 = 1.6$ with heterologous vaccine.

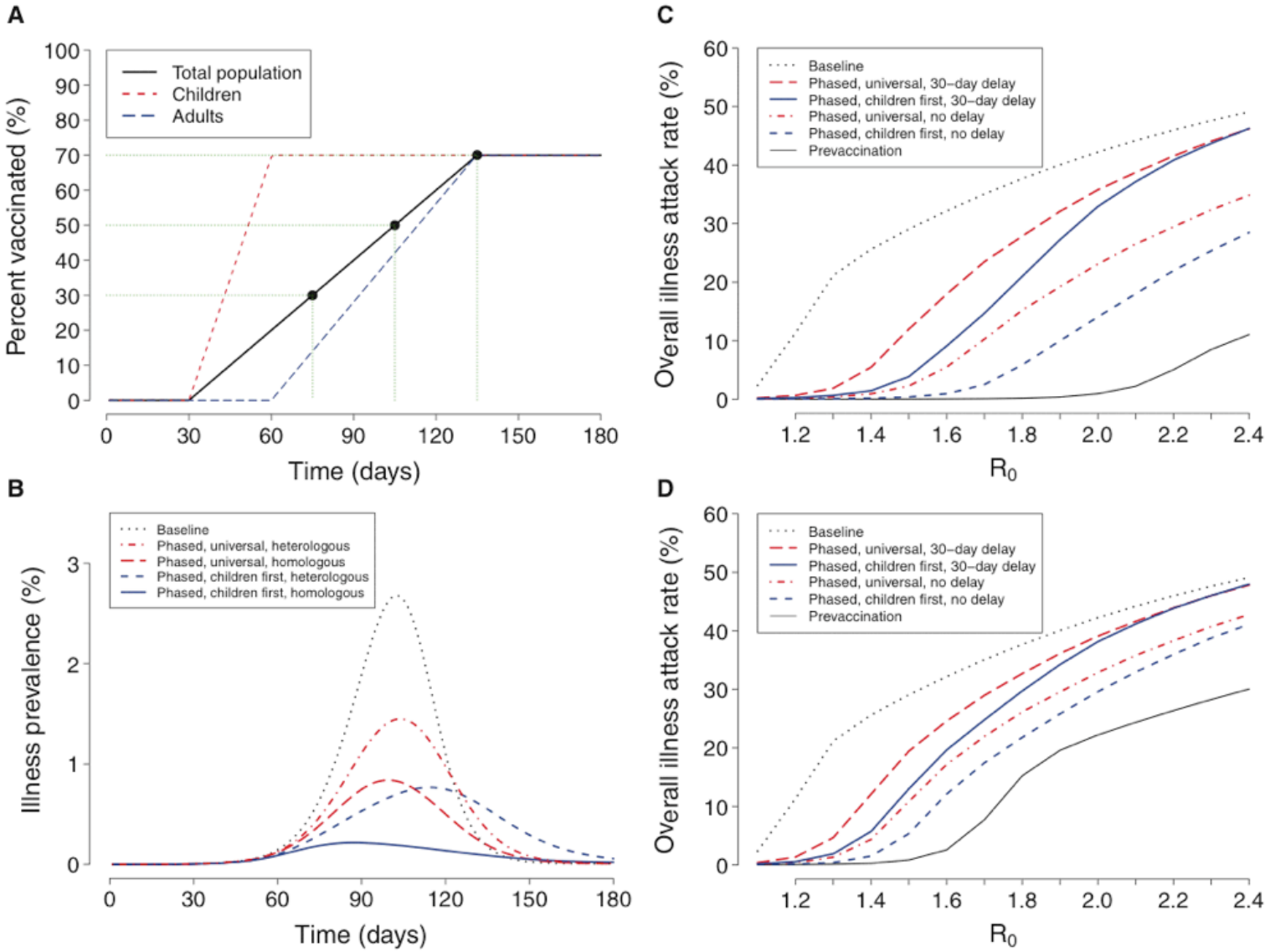

Fig. 5. Simulated effect of phased pandemic influenza vaccination for homologous and heterologous vaccines at different values of R_0 and coverage for the United States. (**A**) Vaccine coverage over time with a 30-day delay. Vaccine is delivered at a rate of 120 million doses each month or about 20% coverage per month. This is enough vaccine to give 60 million people with two doses, 3 weeks apart per month. Vaccine is delivered uniformly over the month. Day 0 is the beginning of pandemic H1N1 spread in the United States. When there is no delay in vaccine supply, vaccination would start on day 0. The dotted lines show the coverage for a strategy to vaccinate children first (red) and then adults (blue) starting when coverage reaches 70% in children. (**B**) Epidemic curves when $R_0 = 1.6$ for homologous and heterologous vaccines, delivered with a 30-day delay. Both universal and the children-first vaccination strategies are shown. (**C**) Overall illness attack rates for homologous vaccine for the universal and children-first vaccination strategies, both with and without the 30-day delay. (**D**) Overall illness attack rates for heterologous vaccine for the universal and children-first vaccination strategies, both with and without the 30-day delay.

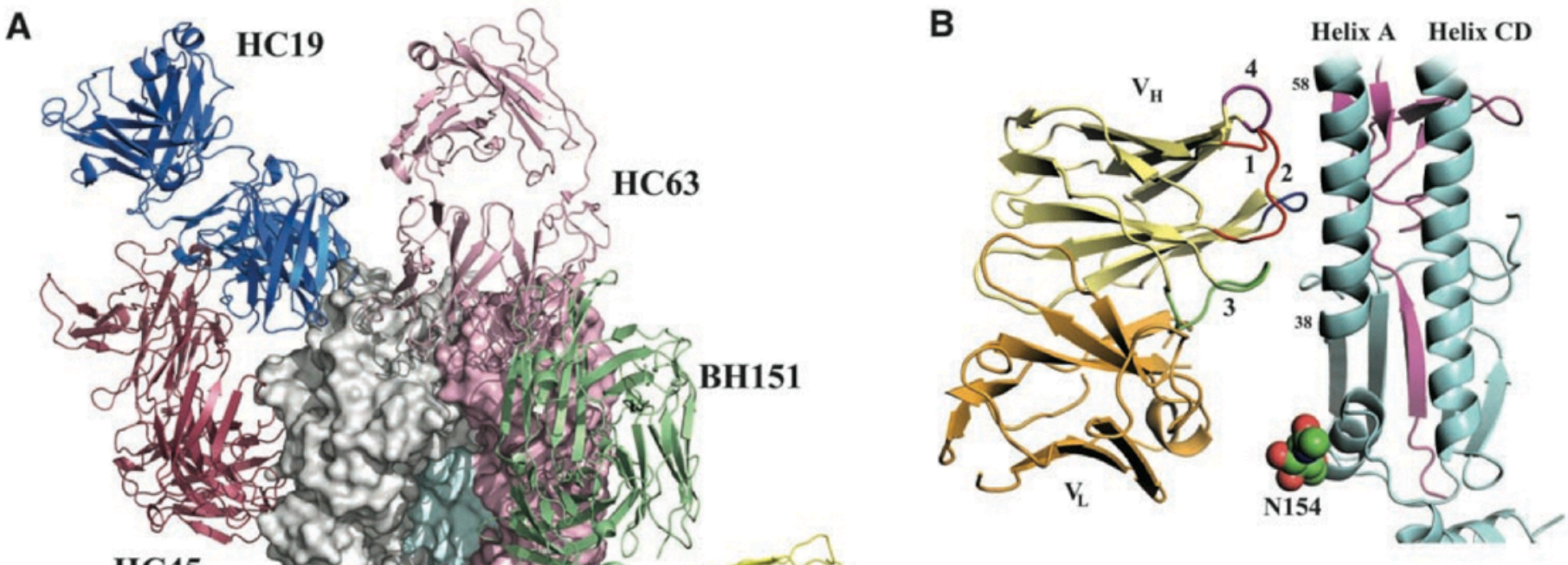

Fig. 2. Broadly neutralizing CR6261 binds in the HA stem distant from other strain-specific antibodies by using only its heavy chain. (**A**) Comparison of the binding sites of Fab CR6261 (yellow and orange, as in Fig. 1) that recognizes the HA stem and strain-specific antibodies that bind to the HA1 globular head domain. The strain-specific antibody structures are depicted in green (BH151, PDB code 1EO8), copper (HC63, PDB code 1KEN), dark red (HC45, PDB code 1QFU), and blue (HC19, PDB code 2VIR). The HA trimer is shown as a surface representation, with the HA1 and HA2 from one protomer colored in purple and cyan, respectively. (**B**) A close-up view of the interaction of CR6261 with the A helix. HA1 and HA2 are colored in purple and cyan, respectively. The HCDRs 1, 2, and 3 of the CR6261 V_H domain are highlighted in red, blue, and green, respectively. In addition, the 72–73 loop from FR3 of V_H, which is structurally analogous to the CDR HV4 of a TCR, is indicated in purple. CDR1 runs along the side of the A helix, interacting with five consecutive helical turns. In contrast, the light chain makes no contacts with the HA and is separated from the nearest HA side chain by ~8 Å. The N-linked carbohydrate attached to Asn^{154} (N154) that prevents the light chain from making contact with the HA is shown in red (oxygen) and green (carbon) balls.